Commissioning of a gantry beamline with rotator at a synchrotron-based ion therapy center

M. T. F. Pivi,[1,*] L. Adler,[1] G. Guidoboni,[1] G. Kowarik,[2] C. Kurfürst,[1] C. Maderböck,[1] M. Pavlovič,[3] D. A. Prokopovich,[1] M. G. Pullia,[4] V. Rizzoglio,[1] and I. Strašík[1]

[1]*EBG MedAustron GmbH, Marie-Curie-Straße 5, 2700 Wiener Neustadt, Austria*
[2]*GKMT Consulting e.U., Argentinierstraße 71, TOP12, 1040 Vienna, Austria*
[3]*FEI STU, Ilkovičova 3, 81219 Bratislava, Slovak Republic*
[4]*CNAO Foundation, Str. Campeggi 53, 27100 Pavia, Italy*

(Received 31 March 2023; accepted 18 January 2024; published 26 February 2024)

This paper provides an overview of the worldwide first commissioning of a gantry beamline with a rotator at the MedAustron synchrotron-based proton/ion cancer therapy facility in Wiener Neustadt, Austria. The gantry beamline consists of the high energy beam transfer (HEBT) line and the gantry beam transport system. It transports the beam from the synchrotron to the gantry-room isocenter. The HEBT transports the beam from the synchrotron to the gantry entrance, which is the coupling point between the HEBT and the gantry. The rotator is one of the HEBT modules, thus it is an integral part of the gantry beamline. The MedAustron rotator is the worldwide first rotator system used to match slowly extracted asymmetric beams from the synchrotron to the rotating gantry. In this paper, main attention is paid to ion-optical and beam-alignment aspects of the beamline commissioning. A novel orbit-correction and beam-alignment technique has been developed specifically for the beamline with the rotator. While the theoretical concept of the rotator has existed for almost two decades, the MedAustron rotator is the first hardware implementation of this concept all over the world. The presented overview of the beamline commissioning includes a description of the principal technical solutions and main results of the first beam-transport measurements. Since the measured beam size and beam position agree well with theoretical predictions, one can conclude that the proof-of-concept of the rotator-matching has been successfully accomplished.

DOI: 10.1103/PhysRevAccelBeams.27.023503

I. INTRODUCTION

MedAustron is a synchrotron-based proton/ion cancer therapy and research facility in Wiener Neustadt, Austria [1–3]. The design of the MedAustron facility originates from the Proton/Ion Medical Machine Study [1] that has been adopted also by the National Center for Oncological Hadrontherapy, Pavia, Italy [4]. This is especially true for the synchrotron ring and extraction technique using the third-order resonance with a betatron core accelerating the beam into the resonance via machine chromaticity [5]. It is partly true also for the layout of the high energy beam transfer (HEBT) line that, of course, had to be adapted to site-specific constraints and requirements of the local medical community. A rendering of the MedAustron facility and the HEBT layout are shown in Figs. 1 and 2, respectively.

The synchrotron with a circumference of 77.6 m delivers proton beams from about 60 to 250 MeV and carbon-ion beams from 120 to 400 MeV/n into three irradiation rooms (IRs) for patient treatment, shown in Fig. 1. The first treatment room IR2 is equipped with a fixed horizontal and fixed vertical beamline intersecting in a common isocenter, the second treatment room IR3 is equipped with a fixed horizontal beamline, and the third treatment room IR4 is equipped with a rotating proton gantry. The gantry room accepts only proton beams up to 250 MeV. All treatment rooms use active pencil-beam scanning (no scattering foils). In addition to the treatment rooms, there is a separate irradiation room IR1 dedicated to non-clinical research. This room is equipped with a fixed horizontal beamline and accepts proton beams up to 800 MeV, which is a limit originated by operating the synchrotron well below the γ -transition energy of 930 MeV [1]. MedAustron is primarily a cancer-therapy center, but it also provides infrastructure installations for external research institutes. MedAustron's basic parameters and beam specifications for cancer therapy are summarized in Tables I and II.

*Corresponding author: mauro.pivi@medaustron.at

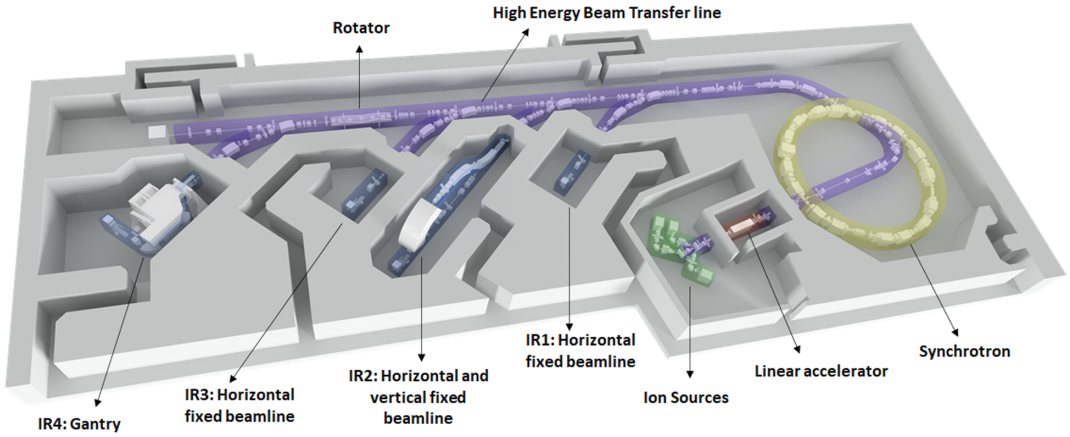

FIG. 1. Overview of the MedAustron facility including the ion sources, the LINAC first stage of acceleration, the synchrotron, the extraction to the HEBT, and the four irradiation rooms.

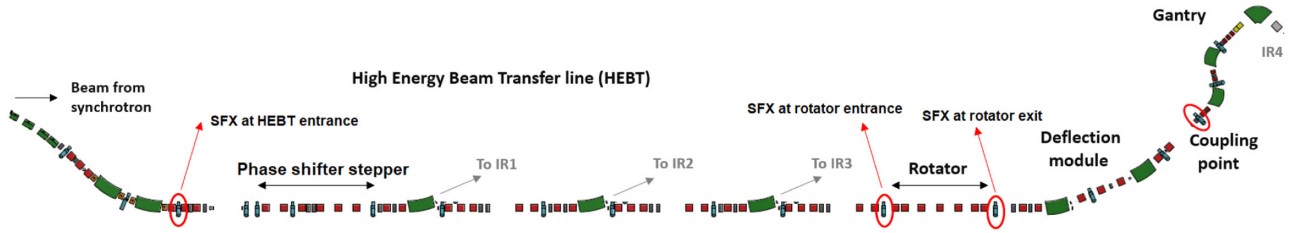

FIG. 2. Layout of the HEBT line including the rotator, the deflection module to the gantry and the rotating gantry. Switching dipoles of the deflection modules to the fixed beamline rooms IR1, IR2, and IR3 are indicated, too. The scintillating fiber hodoscopes (SFX) beam monitors, respectively, at the HEBT entrance and at the rotator entrance and exit, which will be mentioned in this paper, are also highlighted.

Over the last two years, in parallel to clinical operations, we have completed the installation and commissioning of the proton gantry beamline with the first patient treated in May 2022. After the commissioning of the gantry beamline, all irradiation rooms at MedAustron are now in operation. Since the first patient in 2016, about 1400 patients have been treated with protons and carbon ions requiring $\sim 35,000$ single fractions with a weekly machine uptime during clinical operation $>96\%$. The final goal is to reach a patient throughput of 800 patients/year. Figure 3 shows the treatment room of the recently commissioned proton gantry with a rolling floor, robotic patient-positioning system, and exit of the gantry nozzle.

TABLE I. Main MedAustron accelerator and gantry parameters.

Parameter	Value or characteristics
Synchrotron circumference	77.6 m
Maximum beam rigidity	6.37 Tm
Beam extraction technique	Third order resonance via betatron core
γ-transition energy in synchrotron	930 MeV
Gantry type	Barrel-like, isocentric
Magnet technology	Warm
Path-length of the rotating gantry line	15.9 m
Total weight of gantry beamline	$\approx$220 tons
Rotation angle of gantry beamline	$0° \div 180°$

In this paper, we provide an overview of the gantry beamline commissioning including the rotator system as an integral part of the gantry beamline. The rotator is connected to the gantry via an achromatic deflection module with the unit transfer matrix. This configuration has been chosen by MedAustron to match the slowly extracted asymmetric beams to the rotating gantry. Such a beam-transport line has been commissioned for the first time worldwide. Using the rotator, all beam parameters at the gantry isocenter become independent from the gantry rotation angle. The commissioning covered several topics, such as ion-optical aspects, orbit-correction and beam-alignment aspects, performance tests of the rotator, performance tests of the gantry, and, finally, performance tests of the whole beamline. The measured results were compared with computer simulations and an adequate agreement has been found. In this way, the first proof-of-concept of the rotator-matching has been accomplished. The gantry beamline commissioning has been successfully completed and the line is now in clinical operation.

TABLE II. MedAustron basic beam parameters and specifications for cancer therapy. The beam spot-size specification is given in terms of full-width at half-maximum (FWHM) including scattering in the gantry nozzle. Beam intensity is given in particles per spill. The charge-state of carbon ions is 6+.

Parameter	Fixed beamlines	Gantry beamline
Particle species	Protons and carbon ions	Protons
Energy range: protons	62.4 ÷ 252.7 MeV	62.4 ÷ 252.7 MeV
Energy range: C-ions	120 ÷ 402.8 MeV/n	⋯
Spot-size at the isocenter: protons	7 ÷ 21 mm	7 ÷ 21 mm
Spot-size at the isocenter: C-ions	6.5 ÷ 9.5 mm	⋯
Spot-size at the dose delivery system	>6 mm	>6 mm
Maximum beam intensity: protons	2×10^{10}/spill	2×10^{10}/spill
Maximum beam intensity: C-ions	1.5×10^{9}/spill	⋯
Spill length: protons	10 s	10 s
Spill length: C-ions	10 s	⋯
Irradiation field at the isocenter	20 cm × 20 cm	20 cm × 12 cm
Beam delivery at the patient	Pencil-beam scanning	Pencil-beam scanning

II. MATERIALS AND METHODS

A. High energy beam transfer line

The layout of the MedAustron HEBT is schematically shown in Fig. 2. It has a modular structure, although the modular structure as proposed in [6] is not strictly preserved. The HEBT transports the beam from the synchrotron and deflects it either to the research room or to one of three treatment rooms with the aid of achromatic beam-deflection modules. Deflection branches are parallel to each other. Each deflection module contains a switching magnet. With all switching magnets off, the beam is sent to the beam dump. Other MedAustron HEBT modules (phase shifter stepper, rotator, and extension modules) are quite similar to those described in [6]. The beam profile and its position in both horizontal and vertical planes are measured in the HEBT by scintillating fiber hodoscopes (SFX) monitors with a spatial resolution of 1 mm.

FIG. 3. Proton gantry treatment room with rolling floor, automatic robotic patient-positioning system with patient couch, and exit from the gantry nozzle. Gantry angle at 60° (0° gantry angle is defined as the upright gantry position with the output beam pointing vertically downward).

We will refer to the four main energies for commissioning: the minimum energy for clinical use 62.4 MeV, the maximum energy for clinical use 252.7 MeV, and two intermediate energies 136.8 and 198.0 MeV.

B. The rotator

In order to explain the working principle of a rotator, let us assume a situation, when a rotator is inserted directly between the fixed beamline exit and the gantry entrance. In the case of the MedAustron HEBT, there is the deflection module in-between the rotator exit and the gantry entrance (see Fig. 2). Nevertheless, the deflection module is double-achromatic and matched to the unit transfer matrix in both transverse planes of the HEBT, which makes the MedAustron configuration fully equivalent to the simplified model of a gantry connected directly to the rotator exit. The rotator working principle as implemented at MedAustron remains the same—qualitatively as well as quantitively—as if it was implemented without the deflection module.

In general, the rotator is a dispersion-free ion-optical system characterized by the special format of its transfer matrix (the fifth and sixth rows and columns in the matrix are not shown; they are not relevant for the description of the working principle of a rotator):

$$\mathbf{M_{ROT}} = \begin{pmatrix} r_{11} & r_{12} & 0 & 0 \\ r_{21} & r_{22} & 0 & 0 \\ 0 & 0 & -r_{11} & -r_{12} \\ 0 & 0 & -r_{21} & -r_{22} \end{pmatrix}, \qquad (1)$$

where $\mathbf{M_{ROT}}$ is the transfer matrix in the local rotator coordinate system from the rotator entrance to the rotator exit.

When such an ion-optical system is placed in between a fixed beamline and a rotating gantry and physically rotated with respect to the fixed beamline by half of the gantry angle, two coordinate-system rotations appear: the first one between the beamline exit and the rotator entrance and the second one between the rotator exit and the gantry entrance. Let 2α be the gantry rotation angle. The overall transfer matrix $\mathbf{M_{TOT}}$ from the fixed beamline exit to the gantry entrance reads:

$$\mathbf{M_{TOT}} = \begin{pmatrix} \cos\alpha & 0 & \sin\alpha & 0 \\ 0 & \cos\alpha & 0 & \sin\alpha \\ -\sin\alpha & 0 & \cos\alpha & 0 \\ 0 & -\sin\alpha & 0 & \cos\alpha \end{pmatrix} \times \mathbf{M_{ROT}} \times \begin{pmatrix} \cos\alpha & 0 & \sin\alpha & 0 \\ 0 & \cos\alpha & 0 & \sin\alpha \\ -\sin\alpha & 0 & \cos\alpha & 0 \\ 0 & -\sin\alpha & 0 & \cos\alpha \end{pmatrix}. \tag{2}$$

It can easily be shown by performing the matrix multiplication that

$$\mathbf{M_{TOT}} = \mathbf{M_{ROT}} \neq f(\alpha). \tag{3}$$

The transfer matrix from the fixed beamline exit to the gantry entrance is not a function of the gantry rotation angle. Therefore, all individual beam particles have the same coordinates at the gantry entrance independently from the gantry rotation angle. This working principle of the rotator has been known in the literature for two decades [7]. The original proposal appeared even earlier [8].

MedAustron uses a rotator that is a special case of the rotator characterized by the transfer matrix according to Eq. (1). The transfer matrix of the MedAustron rotator is

$$\mathbf{M_{ROT}} = \begin{pmatrix} 1 & 0 & 0 & 0 \\ 0 & 1 & 0 & 0 \\ 0 & 0 & -1 & 0 \\ 0 & 0 & 0 & -1 \end{pmatrix}. \tag{4}$$

It should be noted that this transfer matrix can be converted to the transfer matrix:

$$\mathbf{M_{ROT}} = \begin{pmatrix} -1 & 0 & 0 & 0 \\ 0 & -1 & 0 & 0 \\ 0 & 0 & 1 & 0 \\ 0 & 0 & 0 & 1 \end{pmatrix} \tag{5}$$

just by changing the initial position of the rotator by 90°. Both working regimes of the rotator are fully equivalent.

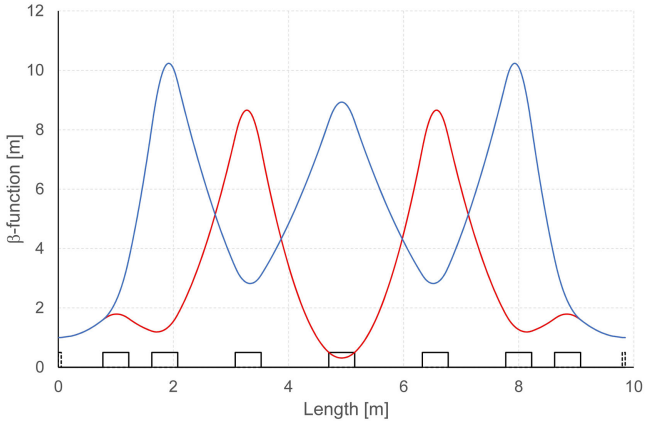

FIG. 4. Lattice functions of the MedAustron rotator in the working regime corresponding to the transfer matrix according to Eq. (4). Red solid line: the horizontal β function, blue solid line: the vertical β function, black solid line: position of the quadrupoles, black dashed line: position of the entrance, and exit SFX monitors.

The MedAustron rotator is a 9.9 m long straight quadrupole lattice containing seven identical quadrupoles (with different strengths) grouped into four families. Three families comprise two quadrupoles each. The two quadrupoles belonging to the same family are placed symmetrically with respect to the longitudinal middle of the lattice. The fourth family has only one single quadrupole located in the longitudinal middle of the lattice, hence keeping its overall longitudinal symmetry. A 20 m long 1:1 achromatic deflection module transfers the beam from the rotator exit to the gantry entrance. Figure 4 shows the lattice functions of the MedAustron rotator in the working regime corresponding to the transfer matrix according to Eq. (4). Figure 5 shows a picture of the MedAustron rotator.

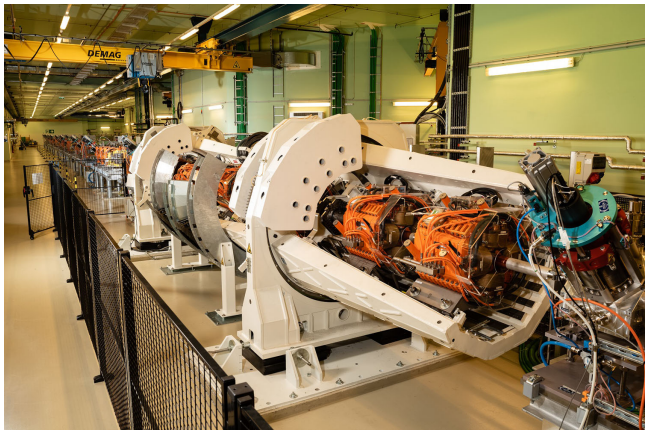

FIG. 5. Worldwide first rotator system (white structure) in the MedAustron HEBT line. Seven quadrupoles (orange) are mounted on a common mechanical supporting structure that is rotated by half of the gantry angle. The gantry is located downstream of the rotator. With the rotator, the beam parameters at the gantry isocenter become independent from the gantry rotation angle.

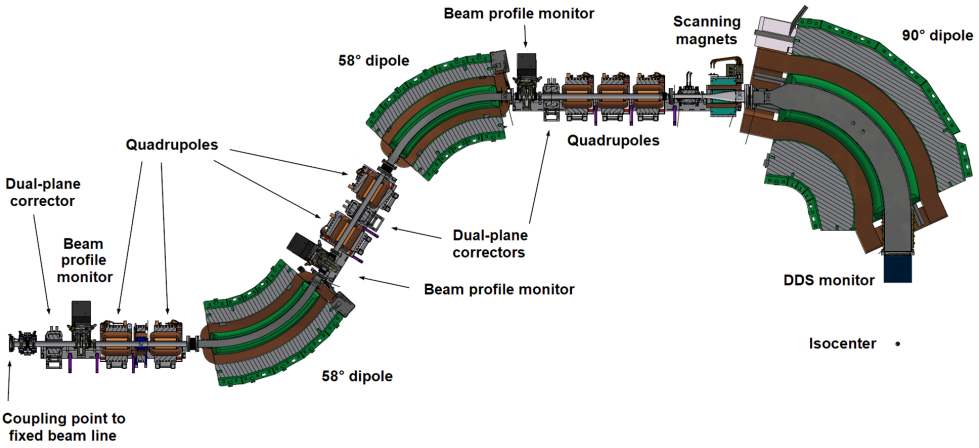

FIG. 6. Beam transport system of the MedAustron gantry (beam entrance from the left).

C. The gantry

MedAustron gantry is based on the Paul Scherrer Institute (PSI) "Gantry 2" design [9,10]. It is a barrel-like isocentric gantry with 2D upstream parallel scanning. No passive beam delivery with beam scattering is used at MedAustron. The beam transport system of the MedAustron gantry is shown schematically in Fig. 6.

The beam transport system of the MedAustron gantry starts at the coupling point with the fixed HEBT and consists of two quadrupole doublets, two 58° dipoles, a final quadrupole triplet, the 90° dipole, and the dose delivery system (DDS) upstream of the patient. The dose delivery system regulates the dose to be delivered to the patient and includes two independent sets of beam monitors: the DDS monitor box 1 (DDM1) and DDS monitor box 2 (DDM2). Further details concerning the gantry nozzle are going to be provided in Sec. III B. Vertical and horizontal scanning magnets are located upstream of the 90° dipole in its focal points to allow for parallel scanning. The position of the 90° dipole focal points is adjusted with the aid of both entrance and exit edge focusing. The precision of the gantry rotation is 0.1°, corresponding to 1.74 mrad. There are three SFX beam profile monitors and three correctors along the gantry beam transport system. Figure 7 shows the MedAustron gantry.

In the preparatory phase of the beamline commissioning, the gantry optics has been studied and predesigned first. The study brought necessary information on the required beam parameters at the gantry entrance that must be served by the HEBT. This information was put together with the existing operational experience gained from running the HEBT with the fixed-beamline treatment rooms.

The gantry optics depends very much on the choice of the matching technique. As far as this point is concerned, the situation at MedAustron was rather special. Since the MedAustron rotator is the first applied rotator worldwide, it was a novel, promising, but nonproven technology. Until the commissioning of the MedAustron rotator, there was no experience with operating rotators. It was advisable to have a technical solution as a backup in the case of unexpected issues would arise when operating the rotator. That was why the gantry-optics studies were based on the so-called sigma-matching optics [11,12] that requires either a point-to-point imaging gantry or a parallel-to-point imaging gantry.

Let us assume a gantry transfer matrix, $\mathbf{R_{GAN}}$, without coupling between the two transverse planes in the gantry local coordinate system (the fifth and sixth rows and columns are not relevant to the description of the gantry imaging modes):

$$\mathbf{R_{GAN}} = \begin{pmatrix} g_{11} & g_{12} & 0 & 0 \\ g_{21} & g_{22} & 0 & 0 \\ 0 & 0 & g_{33} & g_{34} \\ 0 & 0 & g_{43} & g_{44} \end{pmatrix}. \tag{6}$$

FIG. 7. Bird view look at the MedAustron gantry laying in the horizontal position (gantry rotation angle 90°). The gantry entrance is in the lower-right corner of the picture.

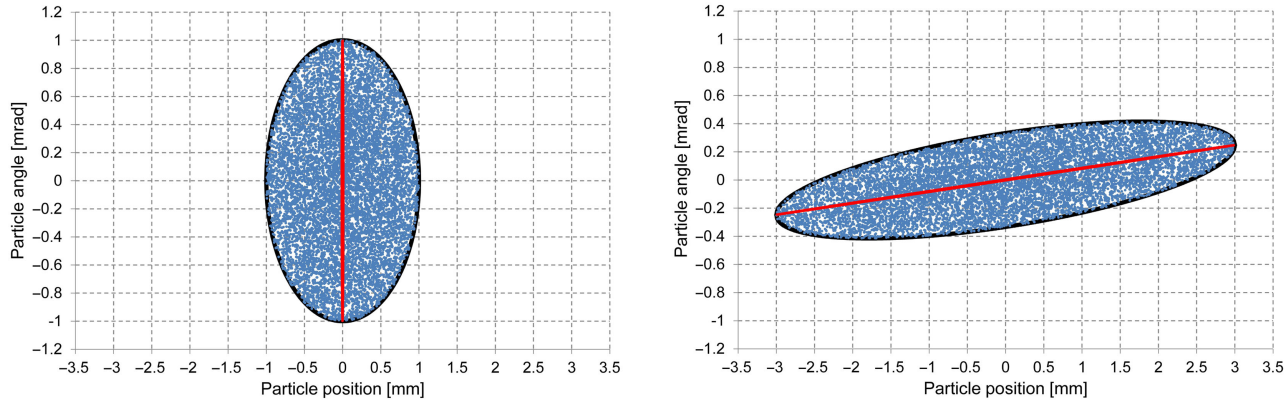

FIG. 8. Illustration of the unfilled ellipse concept and emittance-pattern transformation from the gantry entrance to the gantry isocenter. Left plot: emittance diagrams at the HEBT exit (= the gantry entrance): red dots—the bar in the horizontal HEBT plane, blue dots—the filled ellipse in the vertical HEBT plane, and black line—the rms unfilled ellipse contour hosting the bar and corresponding to $\beta = 1$ m, $\alpha = 0$, and rms geometrical emittance, $\varepsilon = 1\pi$ mm mrad. The particle distributions are cut at 1 rms. Right plot: the corresponding emittance diagrams at the gantry isocenter.

The point-to-point imaging gantry is defined by the transfer matrix terms $g_{12} = g_{34} = 0$. A ray starting from the optical axis at the gantry entrance crosses the optical axis at the gantry exit independently from its input angle. This is equivalent to the gantry phase advance μ satisfying $\sin\mu = 0$ in both gantry transverse planes (the horizontal and vertical phase advances need not be necessarily equal). The parallel-to-point imaging gantry is defined by the transfer matrix terms $g_{11} = g_{33} = 0$. A parallel ray to the optical axis at the gantry entrance crosses the optical axis at the gantry exit independently from its input position. This is equivalent to the gantry phase advance satisfying $\cos\mu = 0$ in both gantry transverse planes for the input-beam waist. Both the point-to-point imaging gantry as well as the parallel-to-point imaging gantry can focus the beam to a round spot at the gantry isocenter independently from the gantry rotation if the beam at the gantry entrance is properly served by the incoming fixed beamline. The point-to-point imaging gantry requires $\sigma_{11} = \sigma_{33}$, whereas the parallel-to-point imaging gantry requires $\sigma_{22} = \sigma_{44}$ at the gantry entrance (σ_{ij} are the sigma-matrix terms of the incoming beam at the gantry entrance). Details and mathematical background concerning the sigma-matching can be found in Refs. [11,12]. Under these circumstances, the MedAustron gantry beamline could be recommissioned and converted quickly to the sigma-matching working regime if necessary. However, with the success of the rotator represented in this paper, this was not necessary. The whole beamline has been tuned, optimized, and commissioned for the originally planned rotator working mode while keeping the sigma-matching gantry optics as an option.

The gantry optics for both imaging modes has been considered. For each imaging mode, several gantry versions with different magnifications have been designed. In the case of the point-to-point optics, the magnification is given by the g_{11} and g_{33} term in the horizontal and vertical gantry planes, respectively. In the case of the parallel-to-point optics, it is given by the g_{12} and g_{34} terms. The same magnification is required in both gantry transverse planes. Many different combinations of gantry magnification and input beam parameters have been studied. Finally, the parallel-to-point optics has been given a priority, because it showed smaller beam envelopes inside the gantry compared to the point-to-point optics. There are still several possible combinations of the gantry magnification and the input beam parameters leading to very similar beam-transport conditions in the gantry. The parallel-to-point gantry with a magnification of 3 m, and input beam Twiss parameters of $\beta = 1$ m and $\alpha = 0$ in both HEBT transverse planes have been finally selected as the most suitable candidate for further studies, optimization, and experimental tests. This choice was based mainly on satisfying the beam specifications at the gantry isocenter as well as at the DDS monitors presented in Table II.

In the vertical HEBT plane, the above quoted Twiss parameters have their standard meaning. In the horizontal HEBT plane, the beam with small horizontal emittance obtained from the slow extraction is depicted by the phase-space points looking like a bar-of-charge in Fig. 8 illustrating the emittance-pattern transformation from the gantry entrance to the gantry isocenter. The bar-of-charge is replaced by a so-called unfilled ellipse with an emittance set to the same value as the vertical one. The ends of the bar are located on the contour of the unfilled ellipse. The horizontal Twiss parameters used to calculate the transport of the bar then correspond to the unfilled ellipse (see Refs. [5,6,13] for further details concerning the bar-of-charge and the unfilled ellipse concepts). The phase advance is used to control the rotation (orientation) of the bar inside the unfilled ellipse.

The bar and the vertical filled ellipse at the HEBT exit satisfy the sigma-matching constraint $\sigma_{22} = \sigma_{44}$. That is

why they produce a round beam spot at the gantry isocenter. This is illustrated in Fig. 8, the right plot. It can be seen that the bar and the filled ellipse give the same rms beam size of 3 mm, which corresponds to the input beam divergence of 1 mrad multiplied by the gantry magnification of 3 m. The corresponding beam FWHM is about 7 mm which fits well to the medical specifications (see Table II). This is the reason why this setting has been chosen as the initial setting for MAD-X simulations and the beamline commissioning.

D. Simulation tools

We used the codes WinAGILE, MAD-X/PTC, and FLUKA for supporting computer simulations [14–18]. WinAGILE was used for a fast and interactive first-order-matrix design and study of the gantry optics as well as for preliminary assessment of the scattering effects in the gantry nozzle that was later refined by FLUKA (see Sec. III B).

MAD-X is a computer code developed for accelerator design, beam optics optimization, particle tracking, and beam dynamics simulation. The particle tracking simulations were performed using the polymorphic tracking code (PTC) module—a symplectic thick-lens tracking routine implemented in MAD-X.

FLUKA is a multi-purpose Monte Carlo software package for the simulation of interaction and transport of particles in matter. It was used to simulate the scattering of the beam particles in the gantry nozzle since the measured beam spot size at the isocenter inevitably contains a contribution from beam scattering. The model implemented in the code is based on the Molière theory of multiple Coulomb scattering. FLUKA is able to simulate also the single scattering using the Rutherford formula. The stopping power of charged particles is calculated using the Bethe-Bloch theory. Inelastic nuclear interactions have been also taken into account in our beam scattering simulations.

III. BEAMLINE COMMISSIONING RESULTS

Beamline commissioning started from the HEBT line with the goal of transporting the beam through the HEBT, the rotator, the deflection module, and the gantry and delivering it to the gantry room with the required parameters at the gantry-room isocenter. The specifications according to medical physics and medical device safety are summarized in Table III. They apply to all beam energies.

Further, the requested beam parameters have been listed in Table II. In this paper, we subdivide the beamline commissioning into ion-optical and beam-alignment parts, although they are closely related to each other.

A. Ion optics

The ion-optical part of commissioning started from the defined Twiss parameters at the gantry entrance which are shown in Table IV. These resulted from underlying gantry ion-optical studies and from the chosen gantry imaging mode (parallel-to-point) as described in Sec. II C. Since the beamline from the rotator entrance to the gantry entrance is performing 1:1/1:−1 beam transport horizontally/vertically, these parameters are required at the rotator entrance as well.

TABLE III. Specifications for the beam parameters at the gantry-room isocenter according to medical physics and medical device safety.

Parameter	Gantry beamline
Beam position at the isocenter	±0.5 mm
Beam position variation during the spill	<0.5 mm
Beam angle alignment with respect to the optical axis	±0.2 mrad
Spot-size roundness: horizontal/vertical profile symmetry	±10% or 1 mm
Spot-size at the dose delivery system (DDS monitors)	>6 mm
Beam position at the scanning system	±1 mm

After measuring the beam profiles at six SFX monitors along the HEBT beamline, the Twiss parameters and the beam phase portraits at the SFX at the HEBT entrance, indicated in Fig. 2, have been determined by the least-square fit of the beam sizes at the monitors with varying the input β function, α parameter, and beam emittance. The HEBT optics has been then matched to obtain an achromatic beamline with $\beta_{x,y} = 1$ m, $\alpha_{x,y} = 0$, and the bar-of-charge oriented "upright" in the phase space at the rotator entrance. The Twiss parameters in the horizontal HEBT plane apply for the unfilled ellipse that contains and describes the bar-of-charge [6,13], as it has been shown in Fig. 8, left plot. The emittances have been refined according to the measurements.

The HEBT optics in terms of the β-functions is shown in Fig. 9. The corresponding beam phase space portraits reconstructed at the SFX at the HEBT entrance and transported to the rotator entrance are shown in Fig. 10. The horizontal planes also show the contour (red curves) of the unfilled "empty" ellipses for 5 rms beam sizes, while the vertical planes show the contour of the normal distribution as well for 5 rms beam sizes. The emittance of the unfilled ellipse in the horizontal plane at the HEBT entrance

TABLE IV. Twiss parameters at the gantry and rotator entrances.

Parameter	Value
Horizontal and vertical β-functions: β_x and β_y	1 m
Horizontal and vertical α-parameters: α_x and α_y	0
Horizontal dispersion and its derivative: D_x and D'_x	0 m/0
Bar-of-charge orientation in the horizontal phase space	Upright

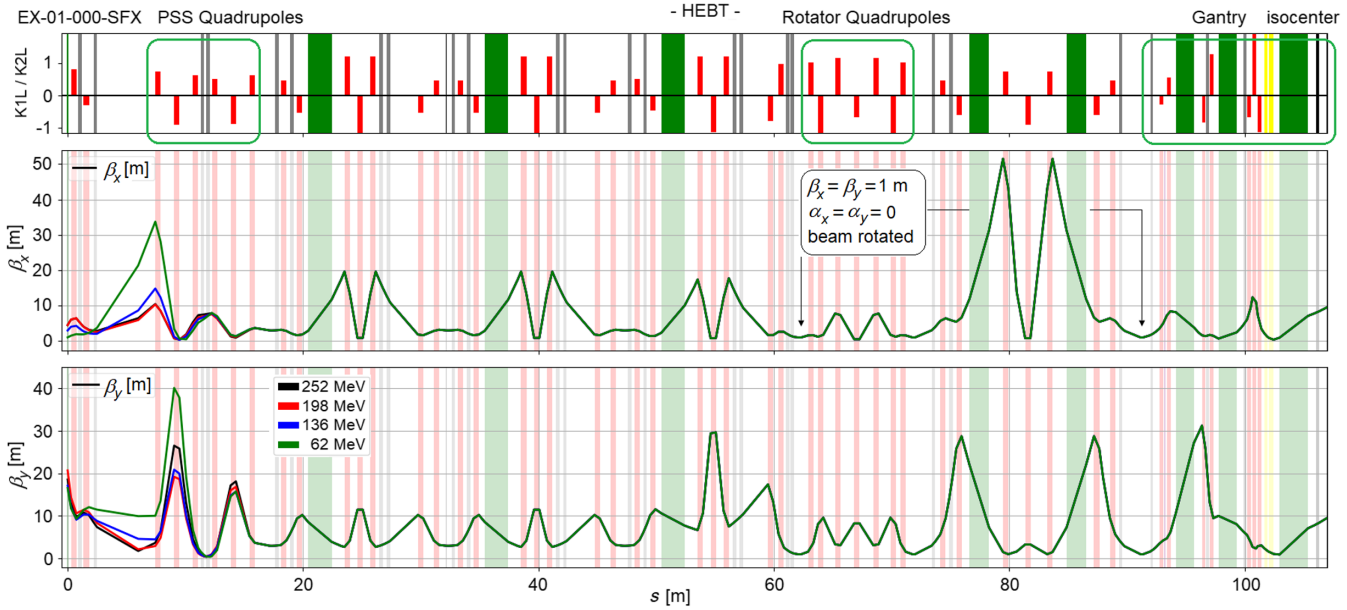

FIG. 9. β functions in the HEBT line up to the gantry isocenter. Main beam transport elements are schematically indicated as follows: red boxes up—horizontally focusing quadrupoles, red boxes down—vertically focusing quadrupoles, green boxes—dipoles, and yellow box—the gantry scanning system. The amplitude of the quadrupole boxes is proportional to the quadrupole strength.

is set to be identical to the full-ellipse emittance of the vertical plane.

It should be noted that normal distributions were applied for populating the emittance diagrams used for tracking. It is an approximation neglecting the special rectangular profile of the bar-of-charge. This approximation is possible thanks to the large amount of scattering of the proton beam in the gantry nozzle, which provides a considerable additional contribution to the beam spot size at the gantry isocenter on top of the optics. This washes out the difference between the rectangular and normal beam profiles.

For the optics matching, the horizontal Twiss parameters correspond to the unfilled ellipse. Its emittance has been selected to be identical to the vertical emittance of the filled ellipse, which is a standard representation of a beam emittance diagram in the phase space. In this way, we have apparently symmetrized (equalized) the horizontal and vertical emittance diagrams into two "identical" ellipses

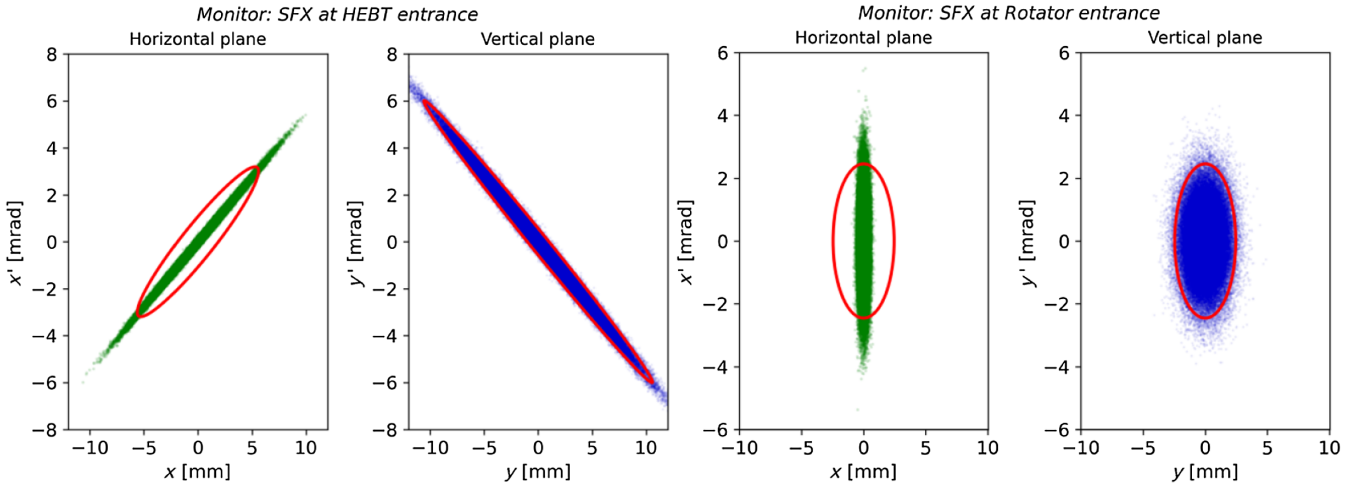

FIG. 10. Beam phase space portraits as reconstructed at the SFX at the HEBT entrance (left two plots) and at the SFX at the rotator entrance (right two plots) after optical matching at 252.7 MeV. The horizontal distribution (bar-of-charge) is standing upright in the phase space at the rotator entrance. The vertical planes show the standard 5 rms beam size ellipses, whereas the horizontal planes show the contours (red curves) of the unfilled empty ellipses with emittance set to the same value as the vertical one. We have plotted the 5 rms beam size ellipses because the 1 rms beam size ellipses would be too small and could not be well recognized together with the particle distribution pattern.

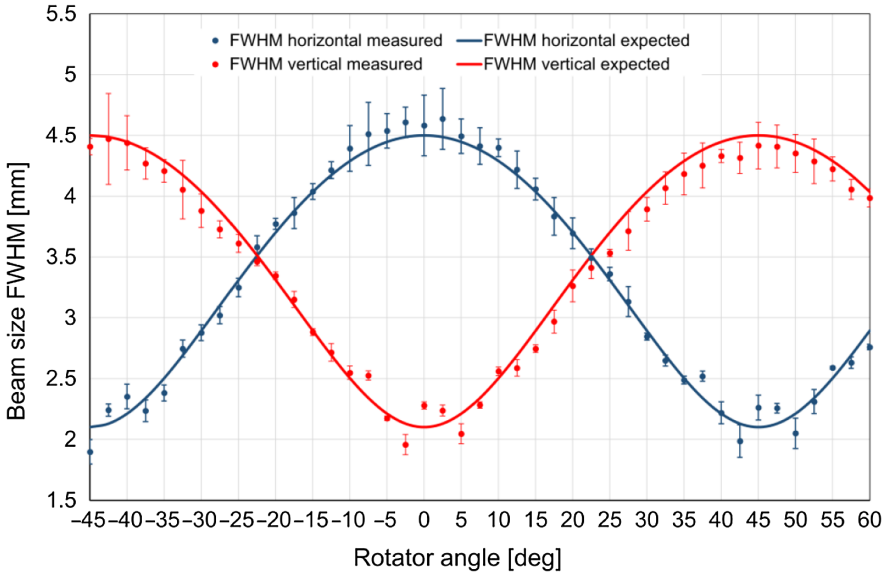

FIG. 11. Horizontal and vertical beam size as a function of the rotator angle at the SFX monitor located at the rotator exit (not rotated with the rotator). Solid lines: theoretical calculation and dots: measured values obtained as an average from four sets of measurements.

at the rotator entrance. In other words, we have obtained the ellipses with identical contours but differently populated with the beam particles. While the vertical ellipse is fully populated, the horizontal ellipse is unfilled and contains the bar-of-charge as its diameter (strictly speaking in the normalized phase space). The orientation of the bar-of-charge inside the unfilled ellipse can be controlled by the horizontal phase advance of the HEBT. The true horizontal geometrical rms emittance of the bar-of-charge is typically ≈1% (order of magnitude) of the vertical one, whereas the emittance of the horizontal unfilled ellipse can be set identical to the vertical one. As a result of the HEBT matching, we have obtained waists with the same projections on the momentum/angle axes in the phase space at the rotator entrance (see Fig. 10, right two plots). Such an input beam is a precondition for the parallel-to-point rotationally independent gantry optics [11,12].

As a part of the optical matching, we have also rematched the rotator section to start/end exactly at the upstream/downstream SFX beam position monitors. According to this change of the coupling point between the rotator and the deflection module located downstream of the rotator, the deflection module has been rematched again to a 1 : 1 transfer matrix for the rotator concept to work.

In the next step, the ion-optical action of the rotator has been thoroughly tested and validated by dedicated beam-size measurements at the rotator exit. For this validation purpose, we have designed a special HEBT optics to serve the beam with an increased horizontal beam size at the SFX monitor at the rotator entrance. This was necessary since, with the nominal optics, the upright bar-of-charge was estimated to be below the spatial resolution of the SFX monitors (∼1 mm given by the fiber thickness and spacing). In order to enable reliable and accurate beam-size measurement, using the special HEBT optics the horizontal beam size has been temporarily enlarged to ∼4.5 mm (FWHM) just for this dedicated experiment.

Figure 11 shows the beam size as a function of the rotator angle α at the SFX monitor at the rotator exit. It must be noticed that the monitor is mechanically detached from the rotating structure of the rotator and does not rotate with the rotator (the same is true for the SFX monitor at the rotator entrance). That is why the SFX monitor at the rotator exit must see the $1:1/1:-1$ beam from the HEBT exit rotated by 2α. It is a direct consequence of the rotator working principle as described in Sec. II B. Realizing this relation helps proper interpretation of Fig. 11.

The beam size behaves as expected. At the rotator angle of 0°, the transverse planes of the rotator receive the beam as formed by the incoming HEBT. As the rotator rotates the beam, the fixed SFX monitor at the rotator exit sees the transition from the horizontal beam to the vertical one in its horizontal plane, and from the vertical beam to the horizontal one in its vertical plane. At the rotator angle of 22.5°, the beam is rotated by 45° and the SFX monitor sees the same beam size in both planes. At the rotator angle of 45°, the beam is rotated by 90°, and the rotator exchanges the horizontal beam with the vertical one at the exit SFX monitor. The measured values are compared with the analytical calculation based on the above-described rotator matrix theory.

After completing the rotator tests, the beam was sent to the gantry. Two gantry optics have been considered and studied: point-to-point optics and parallel-to-point optics. Although both imaging modes are feasible, the parallel-to-point optics has been selected since it fits better to the design constraints imposed on the beam size at the DDS

FIG. 12. Experimental setup in the gantry room during the beam commissioning. The isocenter beam monitor miniQ was mounted on a holder frame connected to the gantry nozzle and rotated with the gantry. Example is shown here for three rotation angles 0°, 30°, and 90°. The miniQ monitor, comprising of a mirror-like window surrounded by a yellow and black frames, is visible on the right picture with gantry at 90° as mounted on its holder frame.

monitor. In addition to this, it also produces slightly smaller beam envelopes inside the gantry, thus providing a larger clearance for the orbit distortions and lower beam losses on the vacuum chamber walls of the gantry.

Beam commissioning was performed for the gantry angles 0°, 90°, and 150° as requested by medical physicists. The beam at 60° gantry angle was also commissioned, but it is currently not clinically used. At present, the gantry angles 0°, 90°, and 150° are clinically available. In the near future, further gantry angles will be commissioned, tested by medical physicists, and available for clinical operation. Figure 12 shows the experimental setup for the beam commissioning at the gantry-room isocenter. Figure 13 presents the measured beam size at the gantry isocenter as a function of the beam energy for the above quoted four gantry angles and the four main beam energies chosen for commissioning.

All the measurements reported in this paper have been performed with scanning magnets set to zero strength.

The beam-spot roundness at the gantry isocenter has also been verified and compared against the requirements. The beam roundness is a measure of the deviation of the beam spot from a circular shape. We have defined it as the relative difference between the horizontal and the vertical beam sizes.

The miniQ-strip monitor is a device designed to monitor the intensity, position, and lateral profiles of therapeutic proton and carbon ion beams. This information comes from the ionization produced in the miniQ-strip box when charged particle beams are passing through it. The monitor is composed of 127 strip channels in each transverse plane with a spatial resolution of 1 mm (strip pitch). During the beam commissioning phase, the miniQ was installed in the irradiation room isocenter to measure the beam parameters.

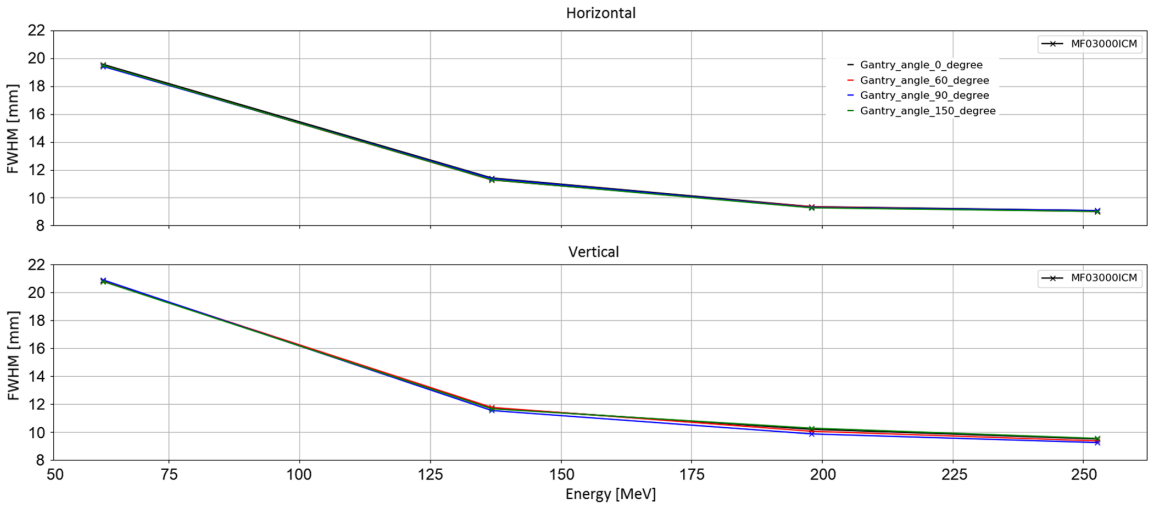

FIG. 13. Horizontal (top) and vertical (bottom) beam size measured at the gantry isocenter as a function of the beam energy for gantry angles of 0°, 60°, 90°, and 150°. The beam size is independent from the gantry rotation angle in both transverse planes. The measurement accuracy is below 4%.

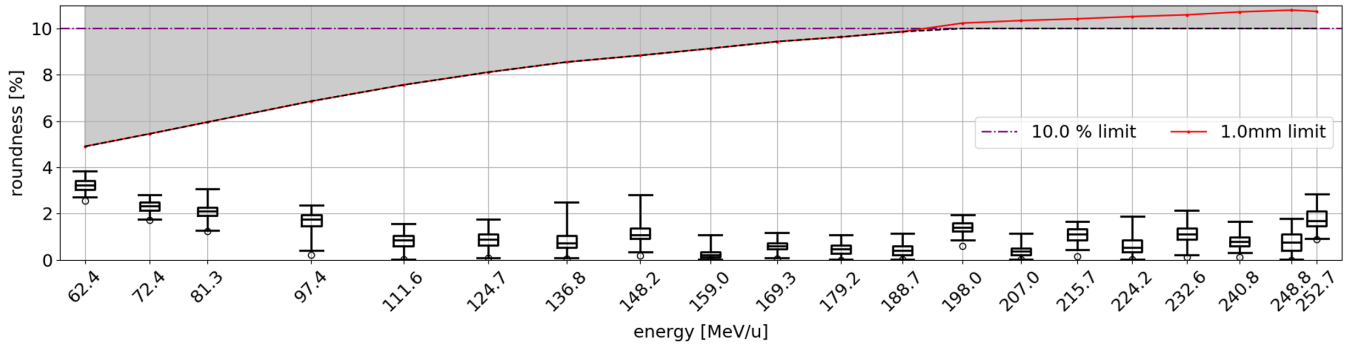

FIG. 14. Measured beam roundness as a function of the beam energy for the gantry rotation angle 90°, together with the specification limits.

It was mounted on a holder frame connected to the gantry nozzle and it was rotated together with the gantry (see Fig. 12).

Technically, the miniQ has a measurement repetition rate of 10 Hz and allows to measure the beam size in terms of FWHM in the horizontal and vertical planes. For a 10-sec-long spill, it performs a total of 100 independent measurements, so-called frames. The average beam size, M_i, for the ith frame is calculated as the mean value from the horizontal and vertical beam sizes. The roundness, R_i, of the ith frame is then calculated as the absolute value of $(S_i - M_i)/M_i \times 100\%$, where S_i is the measured beam size in one of the transverse planes. It should be noted that this beam-roundness measurement technique assumes no coupling between the horizontal and vertical planes at the gantry isocenter, which is justified by the rotator working principle and sigma matching gantry optics. According to our sensitivity analysis, angular misalignments of the rotator and the gantry cause negligible coupling effects only. A Python built-in routine performs statistical analysis of the R_i distribution and yields the corresponding boxplot shown in Fig. 14. The measured roundness has been compared with the specification. The requirement specifies that the difference between the horizontal and the vertical beam sizes at the gantry isocenter shall be within $\pm 10\%$ or within 1 mm, whatever is smaller. The boxplot indicates the minimum and the maximum measured roundness, the median, and the first (lower) and the third (upper) quartiles. The roundness specification is expressed in relative units (percentage) for all energies. This is due to the fact that the beam spot gets larger at low energies due to scattering in the gantry nozzle and in the air. Below about 200 MeV, the 10% relative limit exceeds the absolute limit of 1 mm. Below this energy, the absolute limit is converted to the relative percentage limit resulting in a curve that is decreasing with the beam energy.

As can been seen in Fig. 14, the specification is fulfilled for all beam energies. The measurement was performed at 90° gantry angle. Since the beam size is independent of the gantry angle, as inferred by the measurement presented in Fig. 13, one can expect very similar results for other gantry angles, too. It might be interesting to note that this result was achieved at the first beam-time test using the theoretically calculated optical setting of the gantry beamline. Neither additional tuning nor correcting the theoretical optical setting was necessary.

B. Beam scattering in the gantry nozzle

Beam size (as well as the beam divergence) at the gantry isocenter is enlarged by the beam scattering in the gantry nozzle. This process is energy-dependent, and it is more

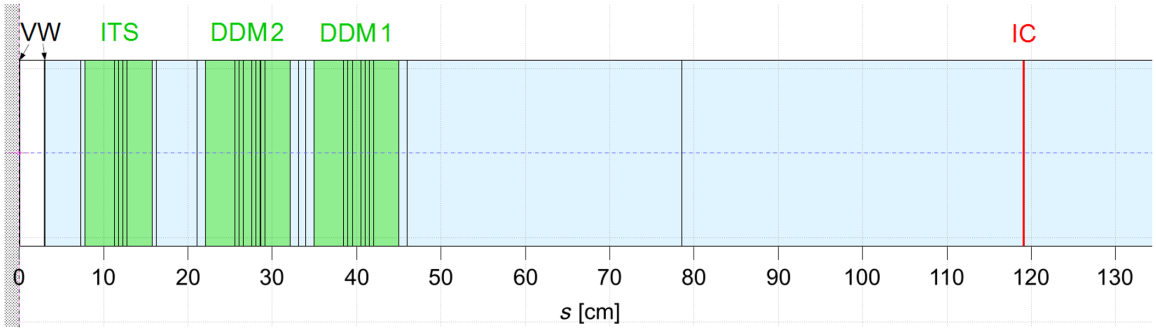

FIG. 15. Schematic representation of the MedAustron gantry nozzle corresponding to its FLUKA model. VW, double-foil vacuum window; ITS, intensity monitor, DDM2 and DDM1, DDS monitors; and IC, isocenter. The vertical lines represent the inner layout of the monitors (their foil structure). The green and light blue colors represent nitrogen and air, respectively.

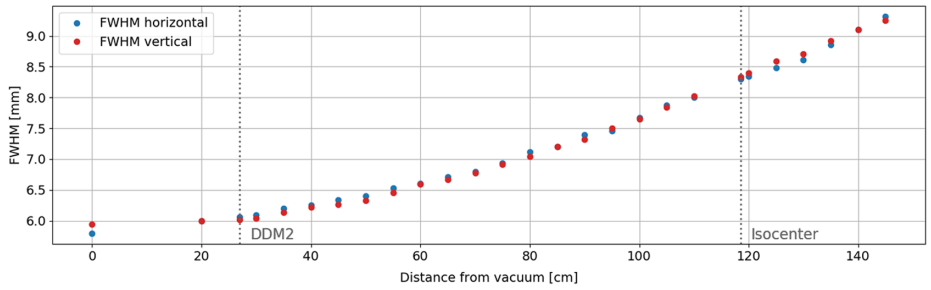

location	longitud. position (cm)	FWHM horizontal (mm)	FWHM vertical (mm)
vacuum window	0.0	5.79	5.94
DDM2	27	6.06	6.02
DDM1	40	6.25	6.22
Isocenter	118.5	8.30	8.34

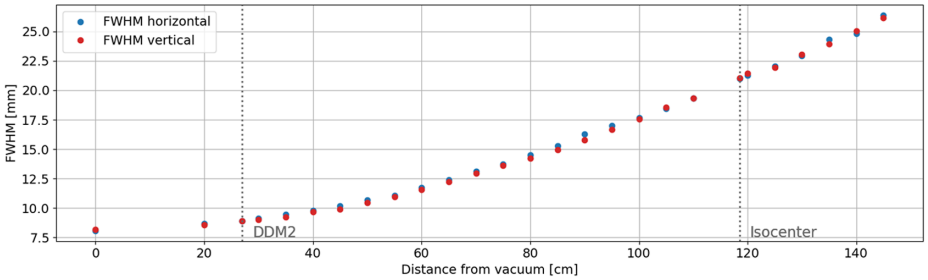

location	longitud. position (cm)	FWHM horizontal (mm)	FWHM vertical (mm)
vacuum window	0.0	8.09	8.18
DDM2	27	8.91	8.89
DDM1	40	9.78	9.66
Isocenter	118.5	21.01	21.03

FIG. 16. FLUKA simulation of the 252.7 MeV (top graph) and 62.4 MeV (bottom graph) proton beam-scattering in the gantry nozzle and air. The "distance from vacuum" stands for the distance from the vacuum-side surface of the double-foil vacuum window terminating the vacuum chamber of the 90° gantry dipole.

pronounced for protons compared to carbon ions. We used beam tracking simulations with the MAD-X/PTC code along the HEBT beamline up to the vacuum window of the gantry to get the beam distribution at the last point of the beamline in vacuum. This beam distribution has been used as an input for the following FLUKA beam-scattering simulations in the dose delivery system located in the gantry nozzle and in the air between the nozzle and the isocenter.

As default settings of the FLUKA code (a set of physical models and data libraries to be used), the default settings HADROTHE [18] suitable for the particle therapy calculations were applied. For the FLUKA simulations, a complete model of the nozzle including all the construction details of the DDS monitors and nozzle geometry has been implemented (see Fig. 15). Particle tracking simulations start from the vacuum side of the double-foil vacuum window terminating the vacuum chamber of the last 90° gantry dipole.

The nozzle is composed of three main beam monitors (starting from the vacuum window): an independent termination system and intensity monitor (ITS), the DDS monitor box 2 (DDM2), and the DDS monitor box 1 (DDM1). Each monitor consists of thin aluminum, Mylar, or Kapton foils and is filled with nitrogen gas. In addition, there is also a nozzle exit window made of Kapton. There are air gaps between the vacuum window and the ITS monitor as well as between the ITS and the DDM monitors. Finally, there is an air gap of about 75 cm from the DDM1 to the isocenter. The total distance between the vacuum window and the isocenter is 118.2 cm.

The initial distribution of the beam particles for the FLUKA simulations is constructed from the outcome of the MAD-X particle tracking simulations in the gantry beamline. The vacuum side of the first foil of the double-foil vacuum window is the "handover" point between the MAD-X and FLUKA simulations (MAD-X output → FLUKA input). Within the FLUKA code, the initial particle coordinates are handed over using the SOURCE subroutine [18].

We performed FLUKA simulations for the four energies used for commissioning. As an example, the simulation results for 252.7 and 62.4 MeV are presented in Fig. 16. Typically, during the simulations, the particle distribution and the beam size (FWHM) in both planes are recorded every 5 cm, as shown in the graphs. The beam particles are tracked up to 150 cm downstream of the vacuum window corresponding to about 30 cm downstream of the isocenter. The numerical values of the beam FWHM at the vacuum window, at the two DDM monitors, and at the isocenter are given in the accompanying table.

The beam-size measurements agree well with the FLUKA simulations (compare Fig. 13 with the numerical values presented in Fig. 16).

C. Beam alignment

Beam alignment in the beamline with a rotator is an entirely new topic. That is why we have chosen a systematic, step-by-step strategy. As a first step, an initial orbit correction was performed along the HEBT beamline from its entrance up to the rotator. In this step, we aimed at minimizing the beam position offset and angle at the rotator entrance. The next goal was to obtain a beam-misalignment invariant with the rotator angle and to avoid beam scraping inside the rotator.

Since the rotator contains no correctors, we have implemented a dedicated method to compensate for the

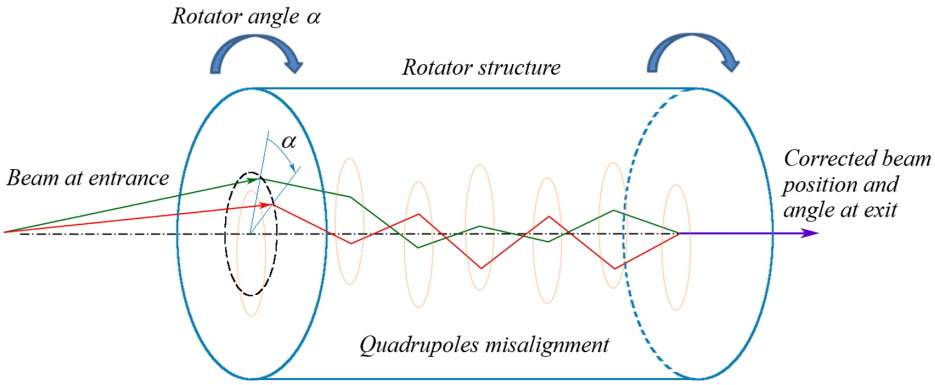

FIG. 17. Principle of the rotator-angle precompensation.

rotator quadrupole misalignments and named it "rotator-angle precompensation." The purpose of the rotator-angle precompensation scheme is to align the beam at the rotator exit for all rotator angles using the upstream HEBT correctors.

Due to the rotator quadrupole misalignments, a perfectly aligned beam at the rotator entrance becomes a misaligned beam at the rotator exit. Conversely, in order to get the beam aligned at the rotator exit, a misaligned beam must be served at its entrance. The rotator-angle precompensation method aims at finding a misaligned beam at the rotator entrance resulting in the aligned beam at its exit, as shown in Fig. 17. In order to keep the output beam aligned for all rotator angles, the misaligned input beam has to follow the rotation of the rotator. This is achieved by making the excitation of the upstream HEBT correctors a function of the rotator angle.

Let us define a corrector-response matrix, $\mathbf{M}$, that maps the correctors' strengths into the required beam positions and angles. At zero rotator angle, the matrix transformation reads

$$\mathbf{X}_0 = \mathbf{M} \times \mathbf{K}_0, \tag{7}$$

where $\mathbf{X}_0$ is the beam vector with the required beam position and angle at the rotator entrance that results in the aligned beam at its exit as shown in Fig. 17 at zero rotator angle, and $\mathbf{K}_0$ is the corresponding set of the corrector strengths. Let us recall that the correctors are located in the HEBT upstream of the rotator.

For a rotator rotation by an angle α, a vector $\mathbf{X}_{\boldsymbol{\alpha}}$ is required at the HEBT exit. It must be identical to $\mathbf{X}_0$ in the rotator local coordinate system, which corresponds to the rotation transformation in the HEBT coordinate system:

$$\mathbf{X}_{\boldsymbol{\alpha}} = \mathbf{R}_{\boldsymbol{\alpha}} \times \mathbf{X}_0, \tag{8}$$

where $\mathbf{R}_{\boldsymbol{\alpha}}$ is the coordinate system rotation matrix. The beam vector $\mathbf{X}_{\boldsymbol{\alpha}}$ can be also derived from the corrector-response matrix $\mathbf{M}$

$$\mathbf{X}_{\boldsymbol{\alpha}} = \mathbf{M} \times \mathbf{K}_{\boldsymbol{\alpha}}. \tag{9}$$

Solving for $\mathbf{K}_{\boldsymbol{\alpha}}$ yields

$$\begin{aligned}\mathbf{K}_{\boldsymbol{\alpha}} &= \mathbf{M}^{-1} \times \mathbf{X}_{\boldsymbol{\alpha}} = \mathbf{M}^{-1} \times \mathbf{R}_{\boldsymbol{\alpha}} \times \mathbf{X}_0 \\ &= \mathbf{M}^{-1} \times \mathbf{R}_{\boldsymbol{\alpha}} \times \mathbf{M} \times \mathbf{K}_0.\end{aligned} \tag{10}$$

This relation provides the transformation of the corrector strengths from zero rotator angle to any rotator angle α once the corrector strengths $\mathbf{K}_0$ for the zero rotator angle are found.

Further details on the theoretical background for this method are going to be published in a dedicated paper.

With this rotator angle pre compensation method, the beam position and angle have been successfully aligned at the rotator exit for all rotator angles. This was inferred on the two SFX monitors downstream of the rotator where plots of the beam position described circles with radii in the order of 200 μm during the rotator rotation. It should be noted that the rotator quadrupoles are aligned by standard mechanical alignment techniques aiming at position accuracy of the rotator quadrupoles less than ±0.1 mm. Since the whole rotator structure is mechanically rotated, asking for over-standard alignment tolerances would make no sense.

As far as the gantry is concerned, the beam misalignment at the isocenter is a superposition of three components: (i) incoming-beam misalignments imaged via the gantry transfer matrix, (ii) permanent gantry-magnet misalignments (independent from the gantry rotation), and (iii) dynamic gantry-magnet misalignments caused by mechanical gantry deformations during the gantry rotation. The dynamic gantry-magnet misalignments depend on the gantry angle. As a consequence, the beam transport in the gantry requires a fine beam-steering procedure for each gantry angle eliminating each of the above-listed components in a step-by-step manner.

That is why the procedure of the beam alignment in the gantry included several steps.

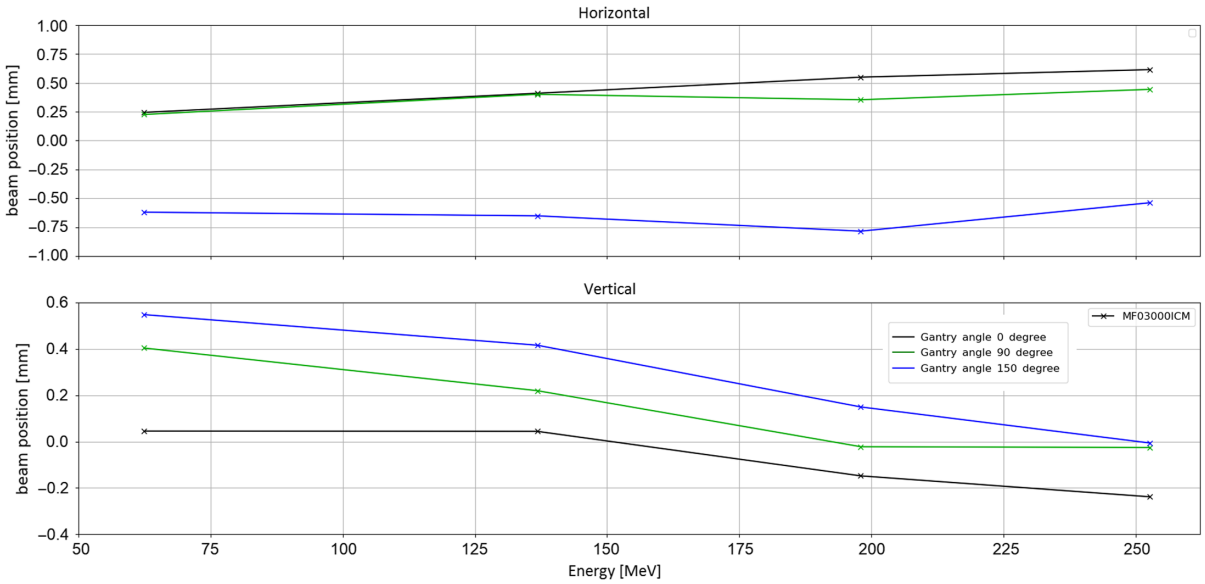

FIG. 18. Horizontal (top) and vertical (bottom) beam position at the gantry isocenter for three different gantry angles and four energies. The beam positions on the monitor depend on the gantry angle due to the monitor shift caused by mechanical deformation of the gantry structure during rotation. The data are corrected for the 7.5 mm horizontal offset caused by the discrepancy between the mechanical and magnetic radius of the last 90° gantry dipole.

In the first step, the beam has been aligned at the gantry entrance. To determine the beam position and the beam angle at the gantry entrance, we applied the quadrupole strength modulation method on the first two gantry quadrupoles and observed the response on the SFX monitors downstream. This method is typically used to determine the beam position offset with respect to the optical magnetic center of a quadrupole. Then to perform the correction of the beam position and the beam angle at this location, upstream correctors have been used to center the beam in the two quadrupoles. This ensures that both the beam position and the beam angle are aligned at the gantry entrance.

In order to keep this alignment valid for all gantry angles, the strength of one of the involved correctors was made a function of the gantry angle. The angular dependence of the incoming-beam misalignments originates from the rotation of the rotator. After the first step, the beam-position differences at the isocenter for all gantry angles were reduced down to about ± 1 mm. As a next step, the beam was aligned at the location of the gantry scanning system using the gantry correctors. Finally, the beam alignment at the isocenter has been completed.

For the beam alignment inside the gantry, we are centering the beam also at selected quadrupole locations in addition to correcting the orbit at the beam position monitors. For this feature, the above mentioned quadrupole modulation strength methods have been integrated into the existing orbit response matrix. Mechanical surveys based on tracking the positions of the quadrupole reference fiducial markers have shown that the permanent quadrupole misalignments are in the order of ≈ 100 μm, which was the alignment goal. This means that the quadrupoles can serve as precise beam-position monitors to follow the beam orbit and to provide information for orbit-correcting actions.

To fulfill the beam-alignment requirements at the scanning magnets, the beam was aligned on the last two quadrupoles located just upstream of the scanning system. Finally, the beam was centered and aligned at the DDS monitors and at the isocenter monitor. For this purpose, the isocenter monitor was mounted on the gantry nozzle and rotated together with the gantry, as shown in Fig. 12. However, rotation of the gantry structure caused mechanical deformations that induced angularly dependent shift of both monitors. That is why these beam-position measurements have been accompanied by mechanical surveys to follow the monitor shift and to apply the corresponding corrections to the target beam positions on the monitors.

Another correction was necessary to compensate for a difference between the mechanical radius and the magnetic radius of the 90° bending magnet originating from a magnet manufacturing imperfection. This difference implied that a well-aligned beam at the entrance of the dipole would exit the dipole with a horizontal position offset of 7.5 mm. Final results of the beam alignment in the gantry in terms of the beam position at the gantry isocenter are shown in Fig. 18 taking into account the 7.5 mm correction for this offset.

IV. DISCUSSION

Initial measurements at the gantry isocenter showed that the horizontal and vertical beam sizes were already within the specifications over the whole energy range and independent from the gantry rotation angle. Therefore, the gantry quadrupole strengths required neither energy-dependent nor

angle-dependent adjustments. Beam-transport and beam-scattering computer simulations were compared with the measured results also at other significant beamline positions, mainly at the rotator entrance, rotator exit, gantry entrance, and gantry exit. The simulations and measurements showed a good agreement. It should be noticed that the commissioning of the proton gantry beamline is, not surprisingly, more complicated than the carbon beamlines. A reason is the presence of the rotating components (the rotator and the gantry), while other beamlines are fixed but also the proton-beam scattering in the gantry nozzle. In the case of carbon ions with less scattering in the gantry nozzle compared to protons, the beam spot size is basically formed directly by the ion optics. On the other hand, the proton beam transport is more challenging since it must also consider the inevitable scattering in the gantry nozzle [19,20]. That is why the beam transport simulations have been completed by scattering simulations in FLUKA. Compensating for the rotator misalignment was another challenge. An original technique has been theoretically developed and practically implemented for the precompensation of the rotator misalignments.

Even though the commissioning of a beamline with rotator is a challenging and complex task, it has been demonstrated in our work that it is feasible. Moreover, it can be successfully accomplished with standard beam-diagnostics and beam-transport systems like the standard SFX monitors, correctors, and magnets (for example, no skew-quadrupoles are necessary). This makes the rotator matching feasible and available for common ion-therapy centers without a need for any special equipment. Combination of the rotator with the rotation-independent (so-called sigma matching) gantry optics is, theoretically, an overdesigned solution. However, it supports the robustness of the whole beamline against various beam-transport imperfections and deviations from the theoretical assumptions and models. This contributes to the reliability of the gantry beamline.

The main results can be summarized as follows.

(i) The ion-optics works as expected. The beam size is essentially independent of the gantry rotation. Neither energy-dependent nor angle-dependent corrections to the ion optics were necessary. The beam-roundness was within the specification. The proof of the rotator concept and its functionality has been validated.

(ii) Concerning the beam alignment, the beam positions at the gantry isocenter are different for each gantry angle, as expected. This is due to the mechanical deformation of the gantry structure during rotation. Correcting for this angular dependence is feasible. With the aid of the orbit correction for each gantry angle, the beam position at the gantry isocenter is within ± 0.5 mm from the target.

In addition, the dependence of the beam spot size on the scanning position has been verified by the Medical Physics group during the acceptance verifications and it fulfills all the requirements, including stability during scanning.

Commissioning of the MedAustron rotator has completed the collection of matching techniques implemented at synchrotron-based ion therapy facilities worldwide [20]. They can be classified into three main categories. Each category represents a different approach to the problem and can be represented by one typical method. The methods representing different categories differ substantially from each other in their working principles.

The first technique exploits a dedicated scattering foil to remove the emittance asymmetry upstream of the gantry entrance. The beam on the foil is shaped in such a way that its emittance diagram in the phase space in the low-emittance plane (usually the horizontal one) is flat (large beam size and small beam divergence), whereas the emittance diagram in the large-emittance plane is upright (small beam size and large beam divergence). Under these circumstances, the emittance blow-up due to the scattering is larger in the low-emittance plane compared to the large-emittance one. The horizontal and vertical emittances get approximately balanced. The energy dependence of the scattering is compensated for by the foil rotation. High-energy beams enter the foil nonperpendicularly to its surface and traverse an effectively thicker foil. More details concerning this technique can be found in Ref. [19]. It is employed, for example, at the HIMAC (Heavy Ion Medical Accelerator in Chiba, Japan) superconducting heavy-ion gantry [21–24].

The second possibility—the rotator matching presented in this work—does tolerate the emittance asymmetry at the gantry entrance but makes it independent from the gantry rotation angle as described in Sec. II B. Because the transfer matrix from the fixed beamline exit to the gantry entrance is not a function of the gantry rotation angle, not only the beam but even all individual beam particles have the same coordinates at the gantry entrance independently from the gantry rotation angle. The rotator matches also the dispersion function since a particle with a certain momentum deviation enters the gantry always at the same position and angle. Originally, the rotator matching was invented for matching the dispersion function in the case of chromatic gantries, for example, the Riesenrad gantry [25,26]. In addition to this, each of the two gantry transverse planes receives the same input beam parameters at all gantry angles. This makes it possible to design the gantry optics in a custom-tailored way based on the input beam parameters, which allows to simplify the optics design and increase its flexibility. The rotator matching principle is very attractive from the ion-optical point of view and offers the most universal technique for removing the angular dependence of the input beam parameters at the gantry entrance.

The third possibility—the so-called sigma-matching—does tolerate the emittance asymmetry as well as the angular dependence of the input beam parameters at the gantry entrance. The matching is subdivided into the incoming fixed beamline and the gantry beamline. The incoming fixed beam line must serve a round beam either in terms of the horizontal and vertical beam size or in terms of the horizontal and vertical beam divergences. The gantry transfer matrix from the gantry entrance to the gantry isocenter (in the local gantry coordinate system) must

perform point-to-point or parallel-to-point imaging, to eliminate the dependence of the output beam parameters at the gantry isocenter on the asymmetric sigma-matrix terms at the gantry entrance. Mathematical background for the sigma-matching can be found in Refs. [11,12]. The sigma matching has been adopted by several gantry designs and gantries in operation [27–33]. The minimum number of gantry quadrupoles needed for this matching technique is six [12], which corresponds to the number of ion-optical constraints imposed on the gantry transfer matrix.

V. CONCLUSIONS

For more than 6 years, patient treatment at MedAustron is ongoing with a continuous ramp-up in the patient throughput toward the final goal of 800 patients per year. MedAustron uses exclusively active pencil-beam scanning in all its treatment rooms. In this beam delivery mode, the ion optics and beam alignment become crucial. Beam commissioning of the proton gantry beamline including the worldwide first rotator has been completed. The commissioning was accompanied by computer simulations. The measured results were compared with the computer simulations and an adequate agreement has been found. This validates several key aspects, namely: (i) the beam model represented by the full ellipse and the unfilled ellipse in the vertical and horizontal HEBT plane, respectively, (ii) the rotator-matching concept, and (iii) the parallel-to-point rotation-independent gantry optics. The gantry beamline was handed over for final testing and certification leading to the first patient treatment in May 2022. Following the gantry beamline commissioning, all rooms at MedAustron are now in operation. The rotator, designed, built, installed, and tested at MedAustron is the first and the only hardware implementation of its kind all over the world. The rotator-matching concept was successfully proven to work resulting in a beam spot at the gantry isocenter to be round and independent from the gantry rotation angle.

ACKNOWLEDGMENTS

We are thankful to Michael Benedikt and Ulrich Dorda for the design of the rotator and the original gantry optics. M. P. acknowledges partial funding from the VEGA Scientific Grant Agency through the Grant No. VEGA 1/0130/20 and would like to acknowledge the support from the European Regional Development Fund, Project No. ITMS2014+: 313011BUH7.

[1] L. Badano, M. Benedikt, P. Bryant, M. Crescenti, P. Holý, A. Maier, M. Pullia, S. Reimoser, and S. Rossi, Proton-ion medical machine studies (PIMMS) parts I and II, respectively, CERN Technical Report Nos. CERN-PS-99-010-DI and CERN-PS-2000-007-DR, 2000, https://cds.cern.ch/record/2858081?ln=en, https://cds.cern.ch/record/2858080?ln=en.

[2] *Das Projekt MedAustron*, edited by T. Auberger and E. Griesmayer (Wiener Neustadt, Austria, FOTEC, 2007), 2nd ed., p. 443.

[3] E. Griesmayer, T. Schreiner, and M. Pavlovič, The MedAustron project, Nucl. Instrum. Methods Phys. Res., Sect. B **258**, 134 (2007).

[4] S. Rossi, The National Centre for Oncological Hadrontherapy (CNAO): Status and perspectives, Phys. Med. **31**, 333 (2015).

[5] L. Badano, M. Benedikt, P. Bryant, M. Crescenti, P. Holý, P. Knaus, A. Maier, M. Pullia, and S. Rossi, Synchrotrons for hadron therapy: Part I, Nucl. Instrum. Methods Phys. Res., Sect. A **430**, 512 (1999).

[6] M. Benedikt, Optics design of the extraction lines for the MedAustron hadron therapy centre, Nucl. Instrum. Methods Phys. Res., Sect. A **539**, 25 (2005).

[7] M. Benedikt and C. Carli, Optical design of a beam delivery system using a rotator, CERN, Geneva, Switzerland, Technical Report No. CERN/PS 96-41 (DI), 1996, https://cds.cern.ch/record/2831063/files/CERN-PS-96-41-DI.pdf.

[8] L. C. Teng, private communications, Fermilab, Batavia, IL Technical Report No. int. rep. LL-134, 1986.

[9] E. Pedroni, D. Meer, C. Bula, S. Safai, and S. Zenklusen, Pencil beam characteristics of the next-generation proton scanning gantry of PSI: Design issues and initial commissioning results, Eur. Phys. J. Plus **126**, 1 (2011).

[10] E. Pedroni, R. Bearpark, T. Böhringer, A. Coray, J. Duppich, S. Forss, D. George, M. Grossmann, G. Goitein, C. Hilbes, M. Jermann, S. Lin, A. Lomax, M. Negrazus, M. Schippers, and G. Kotrle, The PSI Gantry 2: A second generation proton scanning gantry, Z. Med. Phys. **14**, 25 (2004).

[11] M. Pavlovič, A design of a rotating gantry for non-symmetric ion-therapy beams, Nucl. Instrum. Methods Phys. Res., Sect. A **438**, 548 (1999).

[12] M. Pavlovič, E. Griesmayer, and R. Seemann, Beam-transport study of an isocentric rotating ion gantry with minimum number of quadrupoles, Nucl. Instrum. Methods Phys. Res., Sect. A **545**, 412 (2005).

[13] M. Benedikt, P. Bryant, and M. Pullia, A new concept for the control of a slow-extracted beam in a line with rotational optics: Part II, Nucl. Instrum. Methods Phys. Res., Sect. A **430**, 523 (1999).

[14] P. Bryant, AGILE, a tool for interactive lattice design, in *Proceedings of the 7th European Particle Accelerator Conference, Vienna, Austria, 2000*, edited by W. A. Mitaroff, C. Petit-Jean-Genaz, J. Poole, M. Regler, and J. L. Laclare (EPS, Geneva, 2000), p. 1357, https://cds.cern.ch/record/447856?ln=sk.

[15] L. Deniau, R. De Maria, A. Latina, P. Skowronski, and T. Persson (MAD Development Team), MAD: Methodical accelerator design, https://mad.web.cern.ch/mad/.

[16] E. Forest, F. Schmidt, and E. McIntosh, Introduction to the polymorphic tracking code PTC, National High Energy Research Organization (KEK) and CERN Technical Report Nos. CERN-SL-2002-044 and KEK-Report 2002-3, 2002, https://cds.cern.ch/record/573082/files/sl-2002-044.pdf.

[17] C. Ahdida *et al.*, New capabilities of the FLUKA multi-purpose code, Front. Phys. **9**, 788253 (2022).

[18] G. Battistoni, T. Boehlen, F. Cerutti, P. Wai Chin, L. S. Esposito, A. Fassò, A. Ferrari, A. Lechner, A. Empl, A. Mairani, A. Mereghetti, P. G. Ortega, J. Ranft, S. Roesler, P. R. Sala, V. Vlachoudis, and G. Smirnov, Overview of the FLUKA code, Ann. Nucl. Energy **82**, 10 (2015).

[19] T. Furukawa and K. Noda, Compensation of the asymmetric phase-space distribution for a slowly extracted beam from a synchrotron, Nucl. Instrum. Methods Phys. Res., Sect. A **565**, 430 (2006).

[20] J. Y. Tang, L. Liu, Z. Yang, S. X. Fang, and X. L. Guan, Emittance balancing technique for the resonant slow extraction from a synchrotron, Phys. Rev. ST Accel. Beams **12**, 050101 (2009).

[21] Y. Iwata, K. Noda, T. Murakami, T. Shirai, T. Furukawa, T. Fujita, S. Mori, K. Mizushima, K. Shouda, T. Fujimoto, T. Ogitsu, T. Obana, N. Amemiya, T. Orikasa, S. Takami, and S. Takayama, Development of a superconducting rotating-gantry for heavy-ion therapy, Nucl. Instrum. Methods Phys. Res., Sect. B **317**, 793 (2013).

[22] Y. Iwata, K. Noda, T. Shirai, T. Murakami, T. Furukawa, S. Mori, T. Fujita, A. Itano, K. Shouda, K. Mizushima, T. Fujimoto, T. Ogitsu, T. Obana, N. Amemiya, T. Orikasa, S. Takami, S. Takayama, and I. Watanabe, Design of a superconducting rotating gantry for heavy-ion therapy, Phys. Rev. ST Accel. Beams **15**, 044701 (2012).

[23] Y. Iwata, T. Fujimoto, S. Matsuba, T. Fujita, S. Sato, T. Furukawa, Y. Hara, K. Mizushima, Y. Saraya, R. Tansho, N. Saotome, T. Shirai, and K. Noda, Beam commissioning of a superconducting rotating-gantry for carbon-ion radiotherapy, Nucl. Instrum. Methods Phys. Res., Sect. A **834**, 71 (2016).

[24] Y. Iwata, T. Fujimoto, S. Matsuba, T. Fujita, S. Sato, T. Furukawa, Y. Hara, K. Mizushima, Y. Saraya, R. Tansho, N. Saotome, T. Shirai, and K. Noda, Recent progress of a superconducting rotating-gantry for carbon-ion radiotherapy, Nucl. Instrum. Methods Phys. Res., Sect. B **406**, 338 (2017).

[25] M. Benedikt, P. Bryant, P. Holy, and M. Pullia, 'Riesenrad' ion gantry for hadrontherapy: Part III, Nucl. Instrum. Methods Phys. Res., Sect. A **430**, 534 (1999).

[26] S. A. Reimoser and M. Pavlovic, Engineering design and study of the beam position accuracy in the "Riesenrad" ion gantry, Nucl. Instrum. Methods Phys. Res., Sect. A **456**, 3, 390 (2001).

[27] H. Owen, A. Lomax, and S. Jolly, Current and future accelerator technologies for charged particle therapy, Nucl. Instrum. Methods Phys. Res., Sect. A **809**, 96 (2016).

[28] E. W. Collings, L. C. Lu, N. Gupta, and M. D. Sumption, Accelerators, gantries, magnets and imaging systems for particle beam therapy: Recent status and prospects for improvement, Front. Oncol. **11**, 737837 (2022).

[29] H. Owen, R. MacKay, K. Peach,and S. Smith, Hadron accelerators for radiotherapy, Contemp. Phys. **55**, 55 (2014).

[30] H. Owen, D. Holder, J. R. Alonso, and R. Mackay, Technologies for delivery of proton and ion beams for radiotherapy, Int. J. Mod. Phys. A **29**, 1441002 (2014).

[31] J. R. Alonso and T. A. Antaya, Superconductivity in medicine, Rev. Accel. Sci. Techol. **05**, 227 (2012).

[32] E. Felcini, G. Frisella, A. Mereghetti, M. G. Pullia, S. Savazzi, M. Pivi, and E. Benedetto, Beam optics studies for a novel gantry for hadron therapy, J. Phys. **2420**, 012098 (2023).

[33] M. G. Pullia *et al.*, Explorative studies of an innovative superconducting gantry, J. Phys. **2420**, 012099 (2023).